ACS APPLIED MATERIALS & INTERFACES

www.acsami.org

Research Article

Competing Dissolution Pathways and Ligand Passivation-Enhanced Interfacial Stability of Hybrid Perovskites with Liquid Water

Huanhuan Zhou, Jingfan Wang, Mingchao Wang,* and Shangchao Lin*

Cite This: *ACS Appl. Mater. Interfaces* 2020, 12, 23584–23594

Read Online

ACCESS | Metrics & More | Article Recommendations | Supporting Information

ABSTRACT: Material instability issues, especially moisture degradation in ambient operating environments, limit the practical application of hybrid perovskite in photovoltaic and light-emitting devices. Very recent experiments demonstrate that ligand passivation can effectively improve the surface moisture tolerance of hybrid perovskites. In this work, the interfacial stability of as-synthesized pristine and alkylammonium-passivated methylammonium lead iodide ($MAPbI_3$) with liquid water is systematically investigated using molecular dynamics simulations and reaction kinetics models. Interestingly, the more hydrophilic $[PbI_2]^0$ surface is more stable than the less hydrophilic $[MAI]^0$ surface because of the higher polarity of the former surface. Linear alkylammoniums significantly stabilize the $[MAI]^0$ surface with highly reduced (by 1−2 orders of magnitude) dissociation rates of both MA^+ and ligands themselves, while branched ligands, surprisingly, lead to higher dissociation rates as the surface coverage increases. Such anomalous behavior is attributed to the aggregation-assisted dissolution of surfactant-like ligands as micelles during the degradation process. Short-chain linear alkylammonium at the full surface coverage is found to be the optimal ligand to stabilize the $[MAI]^0$ surface. This work not only provides fundamental insights into the ionic dissolution pathways and mechanisms of hybrid perovskites in water but also inspires the design of highly stable hybrid perovskites with ligand passivation layers. The computational framework developed here is also transferrable to the investigation of surface passivation chemistry for weak ionic materials in general.

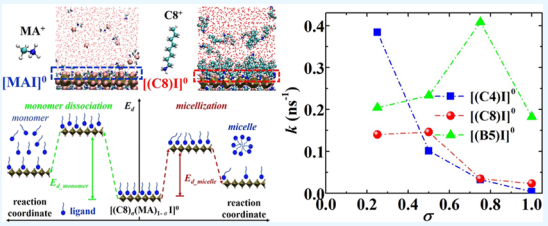

KEYWORDS: *hybrid perovskite, water stability, dissociation kinetics, ligand passivation, micellization*

1. INTRODUCTION

Organic−inorganic hybrid perovskites, $MAPbX_3$ (MA^+ = $CH_3NH_3^+$; X = I, Br or Cl), have emerged as promising light absorbers in photovoltaic (PV) cells[1,2] or as emitters in light-emitting diodes (LEDs)[3,4] because of their scalable and low-temperature synthesis processes[5,6] and superior optoelectronic properties such as strong optical absorption,[7] longer carrier diffusion length (≥1 μm),[8] and high carrier mobilities (≥10 $cm^2/V{\cdot}s$).[9] Despite the enormous progress in device performance of $MAPbX_3$-based PV cells and LEDs, the undesired degradation of $MAPbX_3$ largely hinders the commercialization of $MAPbX_3$-based functional devices. Distinct environmental and operation conditions (*i.e.*, moisture, temperature, and sunlight) may deteriorate the chemical and thermal stabilities of $MAPbX_3$, resulting in the degradation of device efficiency.[10,11] In particular, the moisture effect on the material stability of $MAPbX_3$ is the most research interest because of the inevitable contact with water vapor in the ambient environment.

Various experimental studies have demonstrated the vital role of water molecules in the moisture-induced $MAPbI_3$ degradation.[12,13] For instance, water vapor at room temperature can activate the reversible hydration of $MAPbI_3$ to monohydrate phases of $MAPbI_3{\cdot}H_2O$ or $MA_4PbI_6{\cdot}2H_2O$ (long-time exposure),[14] accompanied by the increased band gap (from 1.6 to 3.1 eV) and hysteresis behaviors.[14] In contrast, liquid water can induce the irreversible decomposition of $MAPbI_3$, releasing PbI_2, CH_3NH_3, HI, and H_2O.[14,15] Such water-induced degradation is also reported to be facilitated by light illumination, which weakens the interaction between inorganic cages PbI_3^- and organic cations MA^+[16,17] and accelerates the irreversible decomposition with increasing humidity levels and light intensities.[9] Despite extensive research on water-induced degradation of $MAPbI_3$, the underlying surface degradation pathway and molecular mechanism at the $MAPbI_3$/water interface are still not well understood.

Recent *ab initio* and classical molecular dynamics (MD) simulations have explored the dynamic interactions of water molecules with different $MAPbI_3$ surfaces and the corresponding impacts on their physical properties. It was found that the MA^+ orientation[18,19] and the terminated surface type (*i.e.*, the charge neutral $[PbI_2]^0$ or $[MAI]^0$)[20,21] play significant roles in

Received: February 24, 2020
Accepted: April 24, 2020
Published: April 24, 2020

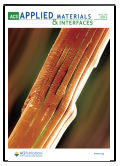

such $MAPbI_3$/water interactions. Specifically, the $[PbI_2]^0$-terminated surface is more robust than the $[MAI]^0$-terminated one which undergoes a rapid dissolution process[20] and forms hydrated compounds $MAPbI_3{\cdot}H_2O$.[21] As a result, the surface degradation widens the band gap by ∼0.3 eV[20] and decreases the optical absorption,[22] giving rise to degradation of the $MAPbI_3$ device performance. However, the time scale of ∼10 ps covered in the above *ab initio* MD simulations may not be sufficient to capture certain water-induced slow surface degradation process. On the other hand, Caddeo *et al.* conducted classical MD simulations to explore the dissolution behavior of $MAPbI_3$ in liquid water and reported an averaged activation energy barrier of 0.36 eV for a $[PbI_2]^0$ monolayer to dissolve.[23] However, the non-integer partial charges of the dissolved Pb and I ions defined in the MYP0[24] and MYP1 potentials[23] might not be compatible with the existing molecular force fields with integer valence charges for the ions, such as CHARMM,[25] AMBER,[26] and OPLS-AA.[27]

In order to suppress the undesired degradation of hybrid perovskites, there are urgent needs to improve their chemical stability and structural integrity at the material level.[28,29] Notably, recent studies have confirmed that surface passivation by organic ligand capping layers (such as long-chain alkylammonium,[30] alkylphosphonic acid ammonium,[31] and phenylalkylamine molecules[32]) or surface covering (such as fluoro-graphene[33]) can effectively stabilize hybrid perovskites by improving their surface moisture tolerance[34,35] and surface hydrophobicity.[30] Moreover, layered or quasi 2D perovskites have shown impressive water resistance compared to 3D ones.[36,37] Linear alkylammonium chains have been used to separate 2D layers of PbI_6^{4-} octahedra composed of central Pb and corner-sharing I atoms, which can stabilize 2D perovskite structures in water.[38,39] Controlling of the peripheral layer of the octahedral perovskite geometry has also been demonstrated to generate water-stable perovskites.[40] However, there is still a lack of theoretical understanding of thermodynamic (*i.e.*, binding energies) and kinetic (*i.e.*, dissociation and association rates) interactions between water molecules and the passivation layers on hybrid perovskites.

With all of the above in mind, we perform classical MD simulations based on a refined empirical potential to investigate the water stability (which is an extreme case of moisture stability when the humidity is above saturation) of $MAPbI_3$ crystals without (original samples) and with surface passivation layers. Both linear and branched alkylammonium ligands were considered for surface passivation at different surface coverages. Our surface ionic dissolution analyses demonstrate, interestingly, that the more hydrophilic $[PbI_2]^0$ surface is more stable than the less hydrophilic $[MAI]^0$ surface because of the higher polarity of the former surface. We also discover that passivated organic ligands can effectively stabilize the $[MAI]^0$ surface even in water. The micellization of ligands, which is due to the hydrophobic nature of the alkyl groups, is found to greatly affect the surface ligand dissolution rate, on top of the impact from their inherent hydrophobicity. Using a parallel reaction kinetics model, we find that such micellization behavior, especially for linear ligands with longer alkyl groups and branched ligands at high surface coverages, dominates and accelerates the dissociation rates of these ligands. Based on MD contact angle calculations, we explore the complex correlation between the surface wettability and the stability of the ligand passivation layers. This computational work provides insightful guidance for searching and designing highly stable hybrid perovskites with organic passivation layers.

2. COMPUTATIONAL METHODS

2.1. Development of an Empirical Potential for $MAPbI_3$/Water/Ligand Systems. The recently developed empirical model potential for hybrid perovskite (MYP0)[24] has been widely utilized to predict multiphysical (structural,[24,41] mechanical,[42] thermal,[43] nucleation,[44] and caloric[45]) properties of $MAPbI_3$. However, the non-integer partial charges are assigned to atoms in the MYP0 potential for $MAPbI_3$ only,[24] and later, the MYP1[24] potential to describe $MAPbI_3$/water interactions are inconsistent with standard valence charges of constituent ions (*i.e.*, I^- and Pb^{2+}).[46] Therefore, we carefully developed a modified MYP potential (referred to as m-MYP hereafter) for $MAPbI_3$/water systems upon refinement of the MYP0 or MYP1 potential. The main differences between the m-MYP and the MYP0 or MYP1 potential include (i) the use of integer partial charges for I^- (−1) and Pb^{2+} (+2) ions and (ii) the revised force field parameters for the Buckingham and Coulombic potentials[46] for the (Pb, I)−(C, N) pairwise interactions. All the parameters of the m-MYP potential (see Table S1 in Supporting Information) were fitted in the GULP[47] package depending on the density functional theory (DFT)-calculated structural and mechanical properties of the $MAPbI_3$ crystal (see Table S2 in Supporting Information). The $MAPbI_3$/water interactions modeled by the m-MYP potential were validated using water contact angle simulations and water adsorption/infiltration energy calculations (see Figure S3 and Table S3 in Supporting Information). The comprehensive validation of m-MYP potential by comparing MD and DFT results were detailedly discussed in Section S1 in Supporting Information.

The SPC/E[48] model (see Table S4 in Supporting Information) was employed for simulating intra and intermolecular interaction of water molecules. The $MAPbI_3$/water interaction was described by the sum of the Lennard-Jones (LJ) 12-6 and Coulombic terms from the AMBER force field.[49] Especially, the rationally-designed LJ parameters for metal[50] and halide[51] ions in explicit solvent were utilized to simulate (Pb, I)/water interaction. The LJ parameters of cross-term interactions were obtained using the common Lorentz−Berthelot mixing rule. Intra and intermolecular interactions of MA^+, two linear alkylammonium ($CH_3(CH_2)_nNH_3^+$, where n = 3 and 7, which are referred to as $C4^+$ and $C8^+$, respectively), and branched alkylammonium ($(CH_3)_3CCH_2NH_3^+$, which is referred to as $B5^+$) cations are described by the AMBER force field[49] as well. The same cut off distances for short-range LJ and Coulombic interactions are set as 1 nm. The partial charges of all alkylammonium ligands were determined from DFT calculations using the B3LYP/6-31G* basis set (see Figure S1 in Supporting Information). The particle−particle particle−mesh (PPPM) method[52] was adopted here to treat long-range Coulombic interaction *via* the reciprocal space because the PPPM method is significantly faster than the regular Ewald summation method.[53] Periodic boundary conditions along all directions were used in all MD simulations.

2.2. MD Simulations of $MAPbI_3$/Water/Ligand Systems. All MD simulations of $MAPbI_3$ crystals with or without ligand-passivated layers in liquid water were carried out using the LAMMPS open-source package.[54] $MAPbI_3$ models were built with a dimension of ∼3.8 × 3.8 × 7.0 nm^3 (about 5000 atoms) based on the pseudo-cubic phase of $MAPbI_3$ (with a lattice constant of 6.3 Å) and two types of charge-neutral surfaces, $[PbI_2]^0$ and $[MAI]^0$. To study the ligand-passivation effects, only $[MAI]^0$-terminated $MAPbI_3$ models were considered. MA^+ cations on the $[MAI]^0$ free surfaces were replaced by $C4^+$, $C8^+$, and $B5^+$ organic ligands to construct ligand-capped $MAPbI_3$ surfaces, referred to as $[(C4)I]^0$, $[(C5)I]^0$, and $[(B5)I]^0$, respectively. Different surface coverages (σ = 25, 50, 75, and 100%) of the $C4^+$, $C8^+$, and $B5^+$ ligands were considered. The $MAPbI_3$ models with and without ligands were then put in contact with the liquid water box (with a dimension of ∼3.8 × 3.8 × 6.2 nm^3 and about 9000 atoms) to cover the top and bottom surfaces. After energy minimization, all $MAPbI_3$/water models were first equilibrated for 2 ns under the *NPT*

https://dx.doi.org/10.1021/acsami.0c03532
ACS Appl. Mater. Interfaces 2020, 12, 23584−23594

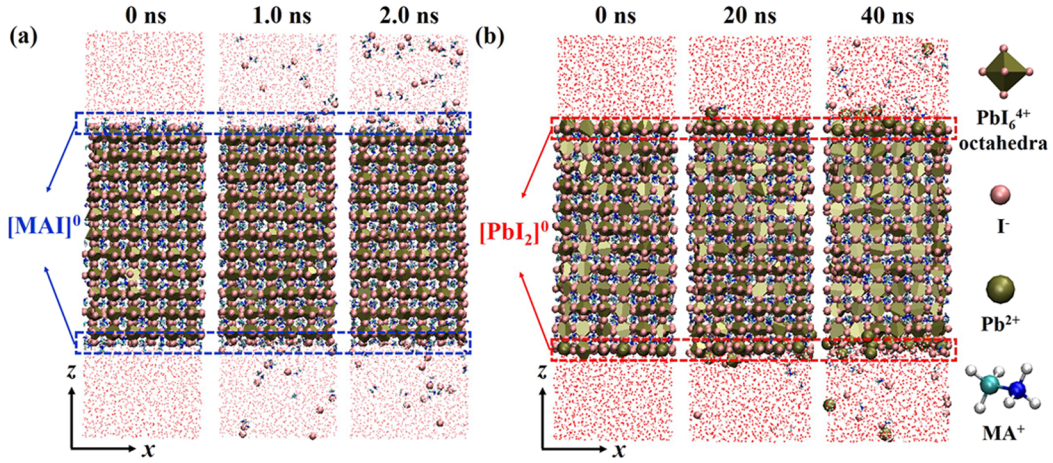

Figure 1. Side views (towards *xz* plane) of the dissociation process of $MAPbI_3$ crystals terminated with (a) the $[MAI]^0$ surface at 650 K and (b) the $[PbI_2]^0$ surface at 800 K. Both free surfaces of $MAPbI_3$ crystals are in direct contact with the liquid water. Owing to different dissociation rates, the atomic configurations of dissociated models are visualized in different ranges of simulation times, including (a) 0−2.0 ns for the $[MAI]^0$ surface and (b) 0−40 ns for the $[PbI_2]^0$ surface. Red denotes O, dark gold denotes Pb, and PbI_6^{4-} octahedra are visualized by triangles that connect all triplets of I atoms within a 3.6 Å radius around Pb.

ensemble using the Nosé−Hoover thermostat and the Parrinello−Rahman barostat[55−57] at a constant pressure of 1 bar and T = 300 K. A time step of 1.0 fs was selected in all MD simulations. All equilibrated $MAPbI_3$/water models were then equilibrated up to 48 ns under the *NVT* ensemble at temperatures ranging from T = 460 to 800 K in order to accelerate the ion dissolution process. The dissolution rates of different ionic species (*i.e.*, MA^+, I^-, Pb^{2+}, $C4^+$, $C8^+$, and $B5^+$) were calculated by tracking the number of dissolved ions in liquid water based on a first-order reaction (dissolution) kinetics model. The corresponding dissolution energy barriers E_d were determined from the temperature-dependent dissolution rates using the Arrhenius law based on the transition-state theory.

2.3. Contact Angle Calculations of $MAPbI_3$/Water/Ligand Systems. To understand the underlying relationship between moisture stability and surface wettability of $MAPbI_3$ crystals, we calculated the contact angles (θ) of water droplets on both bare and ligand-capped surfaces of $MAPbI_3$ at the room temperature. $MAPbI_3$ thin film models with free surfaces were constructed with a dimension of 49.053 × 3.73 × 3.73 nm^3 (~96,000 atoms). They were fully equilibrated under the *NPT* ensemble for 0.1 ns at a pressure of 1 bar and T = 300 K. A liquid water box with 5500 water molecules and a dimension of 12.00 × 3.73 × 3.73 nm^3 was then placed ~0.4 nm above $MAPbI_3$ surfaces to establish the initial contact angle models (see Figure S4 in Supporting Information). The LJ parameters of water molecules used in this study have been listed in Table S4 in Supporting Information. The initial models were equilibrated for 48 ns under the *NVT* ensemble using the Nosé−Hoover thermostat.[56,57] Water contact angles on $MAPbI_3$ substrates were finally extracted from the shape profiles of the equilibrium water droplets.

3. RESULTS AND DISCUSSION

3.1. Dissolution Behavior of As-Synthesized $MAPbI_3$ Surfaces in Water. In order to probe the water stability of as-synthesized pristine $MAPbI_3$ crystals without surface passivation (as a reference case for the passivated surfaces), we studied the dissolution behavior of $MAPbI_3$ thin films with charge-neutral surfaces including $[PbI_2]^0$ and $[MAI]^0$ (see Figure 1). A dissociation cutoff distance (R_{ion}) of ions considering both lattice arrangement (structural) and vibrations (thermal) was utilized to identify dissolved ions (*i.e.*, Pb^{2+}, I^-, and MA^+). The vibration contribution to R_{ion} of each type of ions was determined at different temperatures before any ion dissociation. When the displacement of an ion is larger than R_{ion}, it is recognized as dissociated ion in water, as illustrated in Figure 1. The dissolution profiles of different ions were then obtained by tracking the total number of dissolved surface ions (N_{ion}) as a function of the simulation time. In Figure 2a,b, surface dissolution is rapid at the initial stage and then gradually slows down before reaching complete dissolution (a plateau), which is highly consistent with the first-order reaction kinetics model. Among different ionic species, the dissolution process of the $[MAI]^0$ surface (Figure 1a) is much faster than that of the $[PbI_2]^0$ surface (Figure 1b)

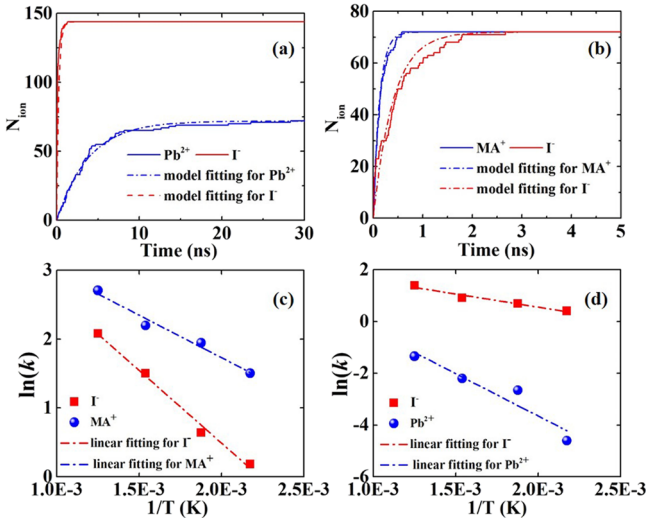

Figure 2. (a,b) Simulated ion dissolution profiles (the total number of dissociated ions N_{ion} with respect to the simulation time) and the fitting curves based on the first-order reaction kinetics model of different ionic species (*i.e.*, Pb^{2+}, I^-, and MA^+) in (a) the $[PbI_2]^0$ and (b) the $[MAI]^0$ free surfaces (including both the top and bottom surfaces in Figure 1) at 800 K. (c,d) Arrhenius plots for the ionic dissociation rates of $MAPbI_3$ crystals (k) with respect to the simulated temperature T, namely, $\ln(k)$ *vs* $1/T$. The dissociation rates k of various ionic species in (a) $[MAI]^0$ and (b) $[PbI_2]^0$ free surfaces are evaluated separately. The dissociation energy barriers E_d of different ionic species can be predicted based on the slopes of the linear fitting curves.

https://dx.doi.org/10.1021/acsami.0c03532
ACS Appl. Mater. Interfaces 2020, 12, 23584−23594

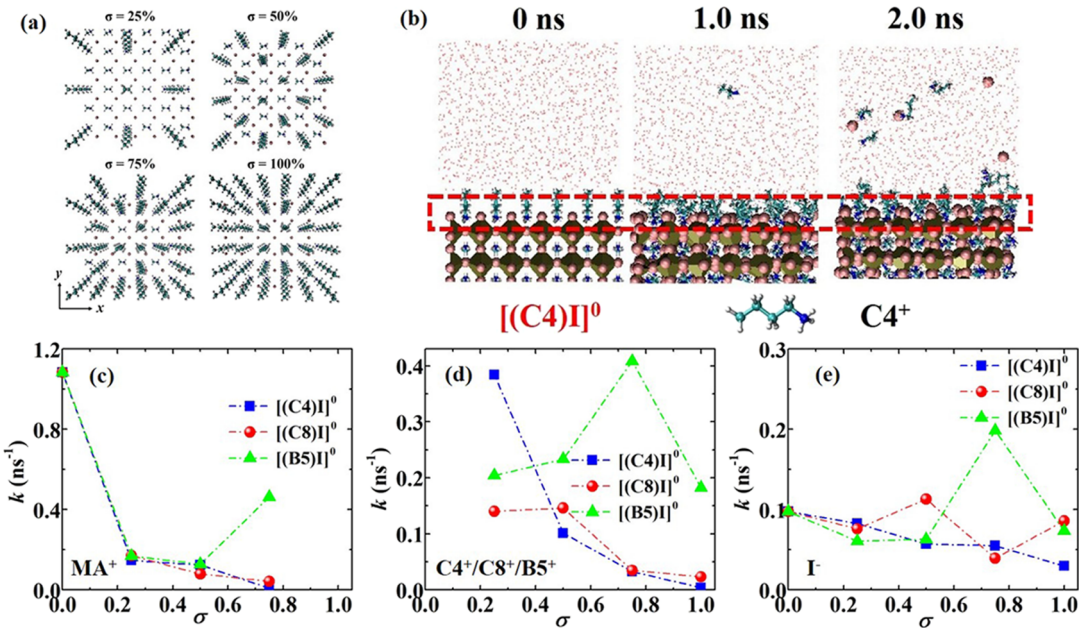

Figure 3. (a) Top views (towards *xy* plane) for the $[MAI]^0$ surface at different surface coverages of $C8^+$ ligands (σ = 25−100%). (b) Side views of the dissociation process of the fully passivated $[MAI]^0$ surface by $C4^+$ ligands (or, namely, the $[(C4)I]^0$ surface) at 650 K, showing highly reduced dissociation rates, as compared to the bare $[MAI]^0$ surface. (c−e) Total dissolution rates (k) of various ionic species from passivation surfaces with respect to σ at 300 K, including (c) MA^+ ions, (d) $C4^+/C8^+/B5^+$ ligands, and (e) I^- ions.

at the same temperature, consistent with the observed surface dissolution profiles in Figure 2a,b.

We then applied a reaction model to explore the different ionic dissolution processes. For a first-order reaction, $kM_{ion} = -dM_{ion}/dt$, with a solution of $M_{ion} = M^0_{ion}\, e^{-kt}$, where M^0_{ion} is the initial number of ions on the $[PbI_2]^0$ or $[MAI]^0$ free surfaces here, M_{ion} is the remaining number of ions staying on the free surfaces, k is the dissolution rate, and t is the simulation time. Therefore, the total number of dissolved ions (N_{ion}) can be predicted by the expression

$$N_{ion} \equiv M^0_{ion} - M_{ion} = M^0_{ion}(1 - e^{-kt}) \quad (1)$$

The dissolution rates k of different types of ions at different temperatures thus can be predicted by fitting their corresponding dissolution profiles to such a first-order reaction model (see Figure 2a,b). The Arrhenius law, $k = C \exp(-E_d/k_BT)$, where T is the absolute temperature, C is the pre-exponential factor, and k_B is the Boltzmann's constant, was then used to fit the dissolution rates k at different temperatures ($\ln(k)$ *vs* $1/T$ in Figure 2c,d) in order to extrapolate k values for different ionic species at the room temperature. The dissolution rates at 300 K were estimated to be 0.098 and 1.08 ns^{-1}, respectively, for I^- and MA^+ ions in the $[MAI]^0$ surface and 0.45 and 3.29×10^{-4} ns^{-1}, respectively, for I^- and Pb^{2+} ions in the $[PbI_2]^0$ surface.

Based on the linear fitting of $\ln(k)$ with respect to $1/T$, we also predicted the dissociation energy barriers E_d of 0.18 and 0.10 eV, respectively, for I^- and MA^+ ions in the $[MAI]^0$ surface and 0.09 and 0.28 eV, respectively, for I^- and Pb^{2+} ions in the $[PbI_2]^0$ surface. We found that I^- ions in the $[PbI_2]^0$ surface have the highest dissolution rate at 300 K, followed by MA^+ ions in the $[MAI]^0$ surface, I^- ions in the $[MAI]^0$ surface, and finally Pb^{2+} ions in the $[PbI_2]^0$ surface. This trend of our results is consistent with the formation energies of vacancy defects in a $MAPbI_3$ crystal, which has been reported in previous study that partial Schottky defects V′(MAI) (0.08 eV) exhibit much lower defect formation energy than V′(PbI_2) (0.22 eV).[58] Overall, the $[PbI_2]^0$ surface is more stable than the $[MAI]^0$ surface in contact with the liquid water, and therefore, the $[MAI]^0$ surface is the weak link in the overall stability of the $MAPbI_3$ crystal. Hydrogen bonds have played very different roles in the stability of hybrid perovskites. The poor surface moisture stability of the $[MAI]^0$ surface can be attributed to the strong hydrogen bonding between MA^+ and water molecules and[59] the increased attractive interactions that drive MA^+ to bind with water molecules. In contrast, similar strong hydrogen bonds have also been utilized to improve the interfacial stability and PV performance of $MAPbI_3$. For example, the strong hydrogen bonds between $[MAI]^0$ surfaces and some carrier transport layers (*i.e.*, TiO_2[60] and $BaSnO_3$[61]) result in ordered orientation of surface MA^+ and promote the electron transfer across the interface.

Using the predicted dissolution rates, we estimated a rate of 5.5 μm/s for the degradation loss of $MAPbI_3$ at 300 K along the thickness direction, consistent with experimental observations that room temperature samples of thickness 1−100 μm degrade in a few seconds.[62] Specifically, we obtained an averaged dissolution rate of $\sim 9.1 \times 10^{-6}$ ns^{-1} per $MAPbI_3$ unit cell (composed of 5 ions in total) at 300 K, assuming a serial reaction kinetics model over all the ionic species (the MD-simulated $[MAI]^0$ and $[PbI_2]^0$ monolayers here are composed of 36 MA^+, 36 Pb^{2+}, and 108 I^- in total). For serial reaction kinetics, the total dissolution times, that is, the summation of $1/k$ over all the ionic species, considering stoichiometry, is used to estimate the averaged dissolution rate. Finally, these lead to an estimated degradation loss rate of 9.1×10^{-6} $ns^{-1} \times$ 0.6 nm = 5.5 μm/s because the lattice constant of pseudo-cubic $MAPbI_3$ is ~0.6 nm.

3.2. Dissolution Behavior of Ligand-Passivated $MAPbI_3$ Surfaces in Water. Surface ligand passivation is one of the most effective strategies to improve the water stability of $MAPbI_3$ under operating conditions.[30−32,35] We explore this strategy to enhance the water stability of the more

https://dx.doi.org/10.1021/acsami.0c03532
ACS Appl. Mater. Interfaces 2020, 12, 23584−23594

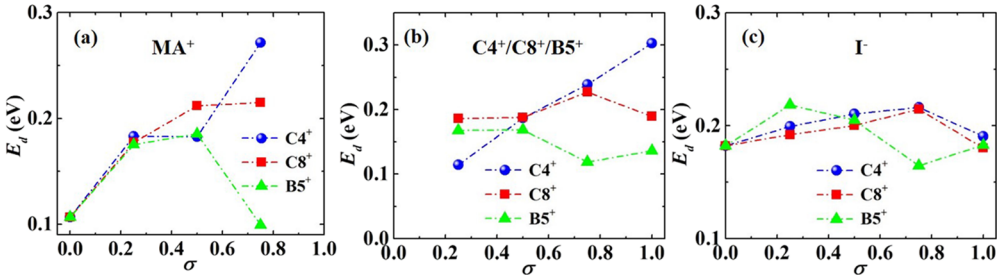

Figure 4. Energy barriers (E_d) against the dissociation of different ionic species in different ligand-passivated surfaces with respect to the surface coverage (σ), including E_d for (a) MA^+ ions, (b) $C4^+/C8^+/B5^+$ ligands, and (c) I^- ions.

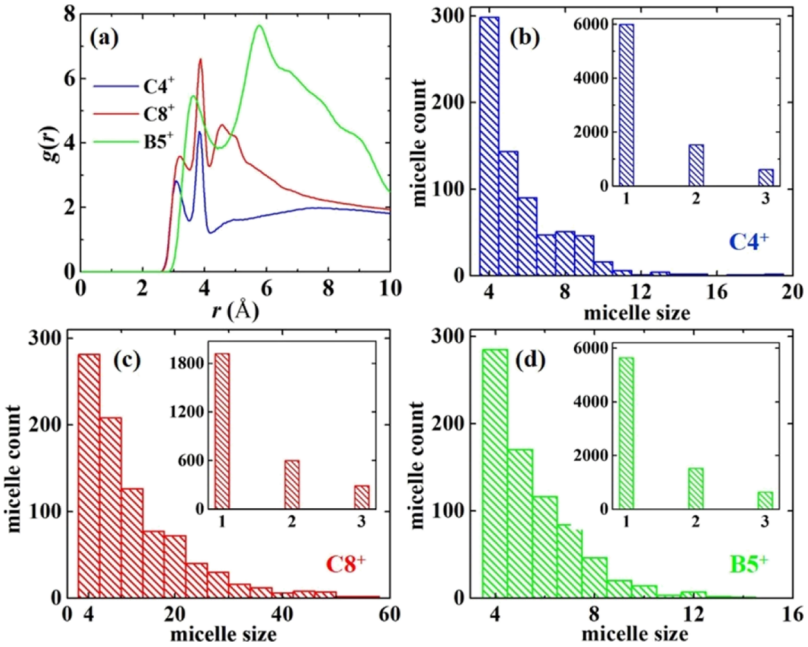

Figure 5. Micellization behaviors of linear and branched alkylammonium ligands dissociated in water. (a) RDFs of intermolecular C−C pairs for $C4^+$, $C8^+$, and $B5^+$ ligands. (b−d) Histograms of the size distributions of micelles composed of dissolved (b) $C4^+$, (c) $C8^+$, and (d) $B5^+$ ligands over the last 2 ns. Insets in (b−d) show the size distributions of monomers (1 ligand molecule) and small micelles composed of 2−3 ligand molecules.

vulnerable $[MAI]^0$ surface to overcome this bottleneck. We then replaced MA^+ ions on the $[MAI]^0$ surface by linear alkylammonium ($CH_3(CH_2)_nNH_3^+$, n = 3 and 7, which are denoted as $C4^+$ and $C8^+$, respectively) and branched alkylammonium ($(CH_3)_3CCH_2NH_3^+$, which is denoted as $B5^+$) ligands at different surface coverages (σ = 25, 50, 75, and 100%) to explore the resulting surface dissolution behaviors in water. In Figure 3a, initial configurations of linear alkylammonium ligands at the above four surface coverages are shown. As an example, the MD-simulated dissociation process of the fully passivated $[MAI]^0$ surface by $C4^+$ ligands (or namely the $[(C4)I]^0$ surface) at 650 K is illustrated in Figure 3b. The ion dissociation rate is significantly reduced upon $C4^+$ passivation (less than 10 $C4^+$ and I^- ions dissociate from the top surface within 2.0 ns of the simulation) as compared to the bare $[MAI]^0$ surface (more than 50 MA^+ and I^- ions dissociate from the top surface within 2.0 ns of the simulation), as shown in Figure 1a.

The total dissolution rates of various ionic species from perovskite surfaces are greatly reduced upon ligand passivation at 300 K and different ligand surface coverages. Figure 3c−e shows that, in general, both $C4^+$ and $C8^+$ reduce (by 1−2 orders of magnitude) the dissolution rates k of MA^+ ions and the ligand themselves and enhance the stability of $[(C4)I]^0$ and $[(C8)I]^0$ surfaces. For example, the MA^+ dissociation rate is reduced from 1.1 ns^{-1} without any ligands (σ = 0) to only 3.51×10^{-2} ns^{-1} with $C4^+$ passivated at σ = 75%, while the $C4^+$ dissociation rate is reduced from 0.32 ns^{-1} at σ = 25% to only 4.53×10^{-3} ns^{-1} at σ = 100%. These results are in good agreement with recent experimental work that the surface passivation of alkyl-chain ligands can effectively improve the water stability of the $[MAI]^0$ surface.[30,35] However, $C8^+$ only reduces the k value of MA^+ ions up to σ = 75% (see Figure 3c). More strikingly, as shown in Figure 3d, the dissolution rate of $C8^+$ even increases with σ at low and intermediate surface coverages. The different dissolution behaviors of linear chain and branched ligands will be discussed later. Figure 3e demonstrates that the k value of I^- ions does not strongly rely on the surface coverage.

In order to further understand the impact of ligand passivation on surface stability, we evaluated the dissociation energy barriers E_d of different ionic species, by fitting all the simulated ionic dissolution profiles of the passivated surfaces based on eq 1 and the Arrhenius law. All the calculated values of E_d (see Figure 4) are consistent with the calculated values of k at 300 K (see Figure 3) in an opposite trend. As shown in

https://dx.doi.org/10.1021/acsami.0c03532
ACS Appl. Mater. Interfaces 2020, 12, 23584−23594

Figure 4a, the dissociation energy barriers E_d of MA^+ ions generally increase with the surface coverage σ of all three types of ligands (note that there are no surface MA^+ ions at σ = 100%). Here, such ligand passivation layer acts as a hydrophobic barrier (will be discussed later) to prevent the $[MAI]^0$ surface from contacting with water and avoid the subsequent surface dissociation. The only exception in the E_d of MA^+ ions is that for $B5^+$, which decreases towards σ = 75%. Figure 4b shows that the $[(C8)I]^0$ and $[(B5)I]^0$ surfaces exhibit better stabilities (larger E_d) of $C8^+$, $B5^+$, and MA^+ than that of $C4^+$ in the $[(C4)I]^0$ surface at a low surface coverage of 25%. At higher surface coverages (σ > 50%), an opposite trend is observed that $C4^+$ protects the free surface better than $C8^+$ and $B5^+$, especially for $B5^+$ which exhibits the lowest E_d among all. With the increase of σ, both $C4^+$ and $C8^+$ show slow increase in E_d, but $B5^+$ shows obvious decrease in E_d, especially at σ = 75%. Such an anomalous dissolution behavior of the $B5^+$ ligand, which shows the smallest E_d among all the ionic species at σ = 75%, will be discussed later. As for I^- ions, Figure 4c indicates that $B5^+$ leads to better stability of I^- ions than $C4^+$ and $C8^+$ do when σ < 50%. Because the dissociation of I^- ion usually accompanies that of the MA^+, $C4^+$, $C8^+$, and $B5^+$ cations, the abilities of the ligands to protect the $MAPbI_3$ surface actually rely on their own stability against water, which will be the focus in our discussion later.[63−65]

3.3. Impact from the Micellization of Dissociated Organic Ligands in Water. To further understand the dissociation process of organic ligands, we monitored their dynamics and found significant aggregations of some dissociated ligands in water (see Figures S5−S7 in Supporting Information). Such dissolution of ligands as aggregates is consistent with previous reports that linear alkyl chains with hydrophilic head groups (charged NH_3^+ here) can dissolve as micelles at the solid−liquid interface,[63−65] and as will be shown later, it plays a significant role in the difference between E_d of $C4^+$, $C8^+$, and $B5^+$ ligands. We next performed radial distribution function (RDF) calculation to investigate the micellization behavior of dissociated surfactant-like organic ligands in water. Figure 5a presents two obvious RDF peaks of intermolecular C−C pairs for organic ligands. Especially, the dominant RDF peaks beyond 0.45 nm reflects the long-range intermolecular ordering among C atoms in organic ligands, demonstrating the micellization of $C4^+$, $C8^+$, and $B5^+$ organic ligands during the dissolution process. The locations of the valley after the first dominant RDF peaks of linear ligands ($C4^+$ and $C8^+$) are at a radial distance of ∼0.42 nm, which is consistent with those reported when studying the micellization of sodium alkyl sulfates.[66,67]

In order to unveil the micellization of organic ligands considered here, we calculated the size distribution of micelles composed of different numbers of dissolved ligand molecules, N_{ligand} (see Figure 5b−d). Ligands dissociated from free surfaces at σ = 100% were taken into account at various simulated temperatures during the last 2 ns of the dissolution simulations. The identification of micelles is determined according to the criterion used by Sammalkorpi *et al.*[66,67] that any surfactant molecule (linear ligand here) with alkane groups within R_{cut} = 0.42 nm belongs to the same micelle. It is important to note that although the primary peak in the RDF of $B5^+$ is located at around 0.6 nm (Figure 5a), this peak actually reflects the strong long-range ordering of the bulky tail groups within a $B5^+$ micelle. In general, to identify micelle formation, one has to monitor the initial contacts between ligands (for $B5^+$, it is reflected by the first peak in the RDF at ∼0.4 nm) rather than the long-range ordering. This is consistent with earlier MD simulation results on other surfactants[66,67] and the linear $C4^+$ and $C8^+$ considered here. Therefore, we set R_{cut} = 0.42 nm to identify micelles for all the ligands considered here to be consistent with each other. Among different types of ligands, $C4^+$ and $B5^+$ ligands prefer to dissolve as monomers (N_{ligand} = 1) or as smaller micelles ($N_{ligand} \leq 3$), and the largest micelle sizes are up to N_{ligand} = 18 for $C4^+$ (Figure 5b) and N_{ligand} = 14 for $B5^+$ (Figure 5d). However, $C8^+$ ligands prefer to dissolve as micelles with larger sizes up to N_{ligand} = 56. This is in good agreement with the higher intensity of the first dominant RDF peaks for $C8^+$ (Figure 5a), confirming that the longer $C8^+$ ligands prefer to dissolve as larger micelles than the shorter $C4^+$ and $B5^+$ ligands.

Owing to the significant impact of micellization on the overall dissociation process of organic ligands, we next proposed a competing dissolution mechanism for organic ligands. As illustrated in Figure 6, organic ligands can be

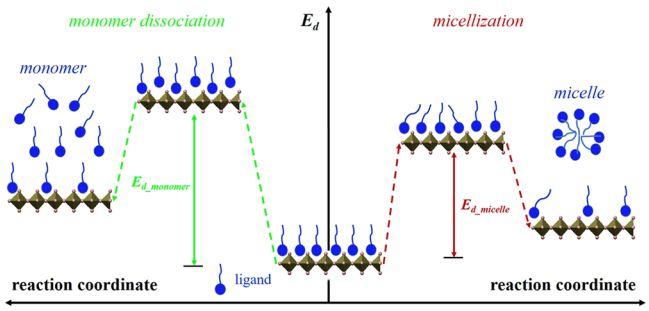

Figure 6. Illustration of the two parallel dissociation pathways and corresponding dissociation energy barrier landscape for the alkylammonium ligands considered here, showing the competition between the fully-dispersed (as monomers) dissolution and the aggregation-assisted dissolution processes. The actual values of $E_{d\_monomer}$ and $E_{d\_micelle}$ are shown in Figure 8a.

dissociated from the passivated free surfaces as monomers and stay fully dispersed in water. Meanwhile, organic ligands possess hydrophobic tails, and they can dissolve as aggregates on the passivated surfaces and directly dissociate into water as micelles. These two parallel competing processes exhibit different activation energy barriers toward the dissociation of ligands as monomers ($E_{d\_monomer}$) or micelles ($E_{d\_micelle}$) from the free surface. We next applied a parallel first-order reaction model to study such competing two-step dissolution process, $A \xrightarrow{k_{monomer}} B$ and $A \xrightarrow{k_{micelle}} C$, where A represents organic ligands on the surface, B represents dissolved ligands as monomers, and C represents dissolved ligands as micelles; $k_{monomer}$ represents the dissolution rate of fully-dispersed ligands as monomers, and $k_{micelle}$ represents the dissolution rate of ligands as micelles. Based on the first order reaction kinetics, we can derive that

$$dM_B/dt = k_{monomer}M_A, \qquad dM_C/dt = k_{micelle}M_A \quad (2)$$

$$\frac{dM_A}{dt} = -\frac{d(M_B + M_C)}{dt} = -(k_{monomer} + k_{micelle})M_A \quad (3)$$

$$M_A = M_A^0\, e^{-(k_{monomer}+k_{micelle})t} = M_A^0\, e^{-kt} \quad (4)$$

https://dx.doi.org/10.1021/acsami.0c03532
ACS Appl. Mater. Interfaces 2020, 12, 23584−23594

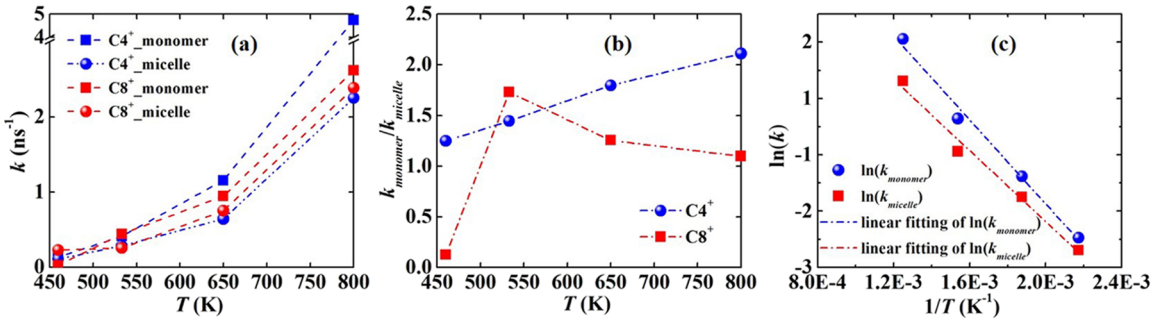

Figure 7. Dissolution kinetics of dissolved ligands as monomers and micelles during the dissolution process of organic ligands in water. (a) Dissolution rates of dissolved $C4^+/C8^+$ as monomers and micelles ($k_{monomer}$ and $k_{micelle}$) at σ = 100%, and (b) their ratio $k_{monomer}/k_{micelle}$ as a function of the simulation temperature T. (c) Arrhenius plot for the dissolution rates of dissolved $C4^+$ as monomers and micelles ($k_{monomer}$ and $k_{micelle}$) with respect to the simulation temperature T, namely, $\ln(k_{monomer})$ and $\ln(k_{monomer})$ *vs* $1/T$.

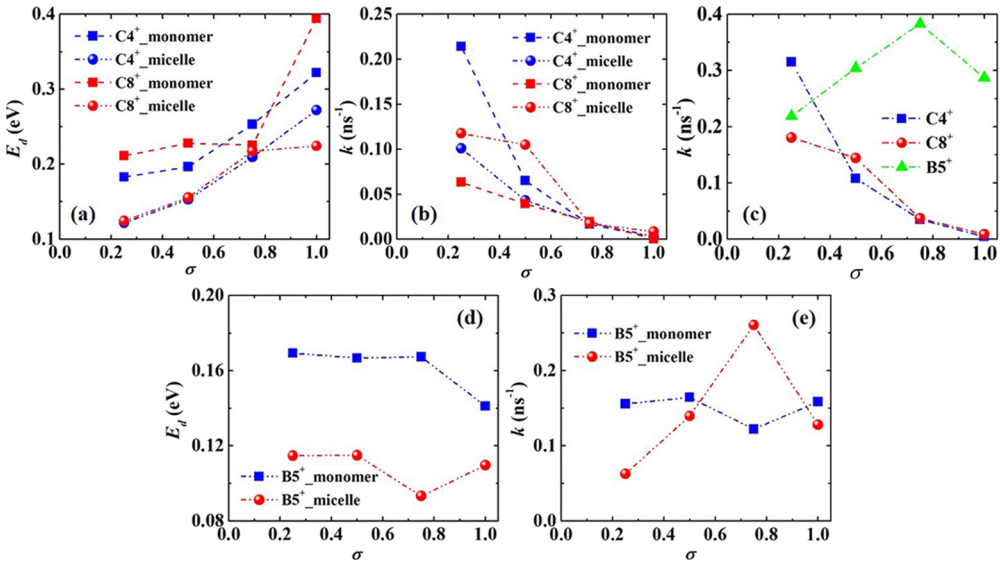

Figure 8. (a) Energy barriers (E_d) and (b) dissolution rates of $C4^+/C8^+$ as monomers and micelles ($k_{monomer}$ and $k_{micelle}$) at 300 K with respect to the surface coverage (σ). (c) Total dissolution rates of $C4^+$, $C8^+$, and $B5^+$ ligands at 300 K, $k = k_{monomer} + k_{micelle}$, with respect to σ. (d) E_d and (e) $k_{monomer}$ and $k_{micelle}$ of $B5^+$ at 300 K with respect to σ.

where M_A is the total number of ligands on the free surface, M_B and M_C are the numbers of dissolved ligands as monomers and micelles, respectively, k is the total dissolution rate for a parallel reaction, and M_A^0 is the initial total number of ligands on the free surface.

According to eq 4, the total dissolution rate $k = k_{monomer} + k_{micelle}$ and k has been already calculation from eq 1. From eq 2, we can derive that $dM_B/dM_C = k_{monomer}/k_{micelle}$ and decouple or separately determine $k_{monomer}$ and $k_{micelle}$ from k by tracking the equilibrium M_B and M_C at the end of the MD dissolution simulation. For instance, at σ = 100%, Figure 7a,b shows that the dissolution of $C4^+$ monomers is always faster than that of $C4^+$ micelles with the increase of temperature, but the dissolution of $C8^+$ as monomers becomes faster only above 500 K. Such difference indicates the effect of the chain length on the competing processes between monomer dissociation and micellization of organic ligands. Based on the Arrhenius law, where $\ln(k_{monomer}) = \ln(C_{monomer}) - E_{d\_monomer}/k_BT$ and $\ln(k_{micelle}) = \ln(C_{micelle}) - E_{d\_micelle}/k_BT$, we can further predict individual energy barriers against the dissolution of ligands as monomers ($E_{d\_monomer}$) and micelles ($E_{d\_micelle}$) (see Figure 7c for the Arrhenius plot for $C4^+$).

Ligand micellization can play a negative role in the surface stability of ligand passivation layers, reflected from the lower energy barriers for ligands to dissolve as micelles ($E_{d\_micelle}$) than as monomers ($E_{d\_monomer}$) for such an aggregation-assisted ligand dissolution process (see Figure 6). Figure 8a,b shows that the energy barriers (dissolution rates at 300 K extrapolated based on the Arrhenius law) for the dissolution of ligands as monomers and micelles increase (decrease) with the surface coverage of ligands σ, except for $C8^+$ micelles at σ = 100% where the dissolution of $C8^+$ as micelles is faster than that of $C8^+$ as monomers. For all ligands, the predicted total dissolution rates k at 300 K based on the parallel two-step reaction kinetics model (see Figure 8c) are close to those predicted directly from the ionic dissolution profiles (see Figure 3d), also validating the accuracy of such parallel two-step reaction kinetics model. At lower surface coverages (σ = 25%), $C4^+$ ligands dissolve faster than $C8^+$ ligands owing to the much higher dissolution rate of $C4^+$ as monomers in water. With the increase of σ, both $C4^+$ and $C8^+$ ligands present similar dissolution behavior. However, at the full surface coverage (σ = 100%), the faster dissolution of $C8^+$ ligands can be attributed to the higher dissolution rate of $C8^+$ as micelles.

https://dx.doi.org/10.1021/acsami.0c03532
ACS Appl. Mater. Interfaces 2020, 12, 23584−23594

Furthermore, we also investigated the dissolution behavior of branched ligand $B5^+$ in water. Different from linear ligands, as shown in Figure 8d, the energy barriers against the dissolution of $B5^+$ as monomers or micelles are nearly independent of the surface coverage, and $E_{d\_monomer}$ is always larger than $E_{d\_micelle}$. Figure 8e shows that the dissolution of $B5^+$ as micelles become faster than that of $B5^+$ as monomers above half surface coverage (σ = 50%), and $k_{micelle}$ reaches the maximum at σ = 75%. This is consistent with the E_d values of different ionic species in the $[(B5)I]^0$ surface which all have the largest E_d at σ = 75%. The total dissociation rate k of $B5^+$ ligands in Figure 8c reveals that $B5^+$ is much less stable than $C4^+$ and $C8^+$ at larger surface coverages, owing to its larger dissolution rate as micelles than the two. This also indicates that surface passivation using $B5^+$ ligands presents the poorest water stability among the three ligands at larger surface coverages.

3.4. Complex Correlation with Wettability of Surface-Passivated $MAPbI_3$ Crystals. Finally, we explored the underlying correlation between the surface wettability and stability of passivated $MAPbI_3$ surfaces with ligand layers. Our contact angle calculations in Figure 9a,b show that the $[MAI]^0$ surface has an approximate contact angle of θ_{MA} = 40 ± 5° (the deviation is due to water dynamics), which is close to experimental measurements,[30] while $[PbI_2]^0$ is highly hydrophilic with a contact angle close to 0°, showing complete wetting. The difference between their wettabilities is in contrast to their corresponding surface stabilities that $[PbI_2]^0$ is more stable than $[MAI]^0$. Although MA^+ ions have hydrophobic CH_3 groups, and therefore, lead to lower wettability of the $[MAI]^0$ surface than $[PbI_2]^0$, water molecules directly weaken the MA^+–I^- interaction, resulting in faster degradation of the $[MAI]^0$ surface than $[PbI_2]^0$. This suggests that the surface wettability (determined by surface ion–water interactions) is not the sole measure of water stability as proposed in earlier studies[30,35] because the later also highly depends on inter-ionic interactions within the solid surface. Furthermore, the wettability of a solid–liquid system depends on both the solid–liquid and the solid–gas (in this case, the interaction between the perovskite surface and a single water molecule) interfacial energies .[68]

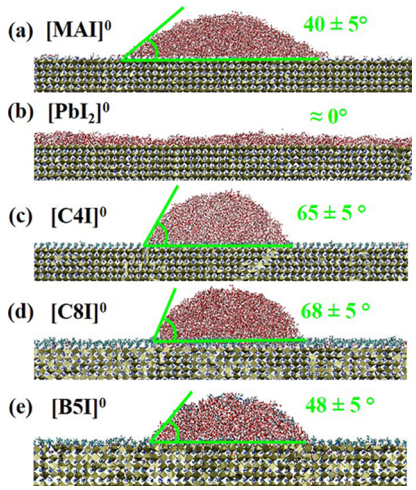

Figure 9. Equilibrium MD simulation snapshots of water droplets on the top of $MAPbI_3$ crystals with different free surfaces, including (a) $[MAI]^0$ and (b) $[PbI_2]^0$ and ligand-passivated surfaces (c) $[(C4)I]^0$, (d) $[(C8)I]^0$, and (e) $[(B5)I]^0$ at full surface coverages (σ = 100%) of $C4^+$, $C8^+$, and $B5^+$ ligands. The values of contact angles for different free surfaces are presented in green.

When $[MAI]^0$ is passivated by different ligands at a full surface coverage of 100%, the predicted contact angles follow the trend: $\theta_{C8} > \theta_{C4} > \theta_{B5}$ (see Figure 9c–e), which is in good agreement with previous studies that the contact angle increases with the chain length (for $B5^+$ the primary chain length is C3).[69,70] Among these ligands, $B5^+$ is slightly longer than MA^+, and thus has a contact angle of θ_{B5} = 48 ± 5° that is close to that of MA^+ (θ_{MA} = 40 ± 5°). In these cases, passivation layers behave as water resisting barriers, which are demonstrated by the very gradual decrease of water densities across these passivation layers (see Figure S8 in Supporting Information). As a result, they further limit the interaction between water molecules and hydrophilic groups (NH_3^+) of ligands, thus improving the surface stability. The hydrophobicity of the passivation layer nearly correlates to their surface stability: the more hydrophobic the alkyl groups in the ligands are, the more resistant they are to surface dissolution. For example, except for branched $B5^+$ which can still cover large areas even at lower surface coverages, larger surface coverages of linear ligands result in stronger hydrophobicity (larger contact angles, see Figures 9 and S9 in Supporting Information for contact angles on passivated surfaces at σ = 50%), and consequently, higher surface stability (lower dissociation rates, see Figure 8). In addition, $C4^+$ and $C8^+$ contribute to more stable free surfaces than $B5^+$ and MA^+ do. However, it is important to note that the aggregation-assisted ligand dissolution process, especially for those with long alkyl chains, can accelerate the surface degradation by their faster dissolution as large-size micelles, in addition to the wettability factor above. Such micellization effect should be considered for the optimal design of ligand passivation layers for $MAPbI_3$.

4. CONCLUSIONS

In summary, we have conducted MD simulation using a refined molecular potential to study the water stability and dissociation pathways of $MAPbI_3$ crystals without and with surface ligand passivation layers. Both linear and branched organic ligands with different surface coverages were taken into account for surface passivation. Based on a reaction kinetics model, our computational results show that $[MAI]^0$ dissolves faster than $[PbI_2]^0$ because of the fast solvation of the organic cation MA^+ by water. Although $[PbI_2]^0$ is more stable than $[MAI]^0$ in water, the former exhibits much greater wettability (smaller contact angles) than the later surface, suggesting that the surface wettability (determined by ion–water interactions) is not the sole measure of water stability as conventionally assumed because the later also depends on inter-ionic interactions within the solid surface. On the other hand, our contact angle calculations of the ligand passivated surfaces do show a positive correlation between surface wettability (inversely correlated with ligand hydrophobicity) and water stability. This suggests that for surfaces passivated by similar chemicals (*e.g.*, alkylammonium ligands considered here), the conventional positive correlation between surface wettability and water stability still holds.

We also demonstrate that passivated linear alkylammonium ligands can effectively stabilize the more vulnerable (as compared to $[PbI_2]^0$) $[MAI]^0$ surface, where the dissociation rates of both MA^+ and ligands are significantly reduced with increasing the ligand surface coverage. In contrast, the

https://dx.doi.org/10.1021/acsami.0c03532
ACS Appl. Mater. Interfaces 2020, 12, 23584–23594

branched ligand surprisingly leads to a higher dissociation rate with increasing the surface coverage, while longer-chain ligands also dissociate faster at the full surface coverage. Using a parallel two-step reaction kinetics model, such anomalous behaviors can be attributed to the aggregation-assisted dissolution of surfactant-like ligands as micelles during the degradation process. Because of the lower energy barriers associated with the ligand aggregation on the surface, ligands prefer to dissociate directly from the surface as micelles into water, rather than dissolving as fully-dispersed monomers as commonly assumed, thus leading to the much higher overall dissociation rates. While the longer-chain linear ligands prefer to micellize at the full surface coverage, the micellization of the branched ligand on the surface can occur at lower surface coverages because of their bulky hydrophobic alkyl groups. Therefore, both longer-chain and branched ligands suffer from the negative micellization-assisted dissociation effect. As a result, we found that a shorter linear chain length of the capping ligand $C4^+$ could lead to the lowest surface dissolution rate. When considering a wider range of chain lengths or branching types beyond the scope of this work, we do expect a complex nonlinear trend between the chain structure and the surface dissolution rate. This results from the competition between (i) water repelling enabled by longer or bulkier hydrophobic ligand tails and (ii) aggregation-assisted self-dissolution of longer or bulkier amphiphilic ligands. This work provides insightful fundamental guidance for searching and designing organic ligand passivation layers for water-resistant organic−inorganic hybrid perovskites. The computational framework developed here could be also transferrable to the investigation of surface passivation chemistry for other weak ionic materials in general.

■ ASSOCIATED CONTENT

Supporting Information

The Supporting Information is available free of charge at https://pubs.acs.org/doi/10.1021/acsami.0c03532.

Details of potential training and validation for $MAPbI_3$ and ligand/$MAPbI_3$/water interactions and parameters of the newly developed m-MYP potential (PDF)

■ AUTHOR INFORMATION

Corresponding Authors

Mingchao Wang − *Department of Materials Science and Engineering, Monash University, Clayton, Victoria 3800, Australia*; Email: mingchao.wang@monash.edu

Shangchao Lin − *Institute of Engineering Thermophysics, School of Mechanical and Power Engineering, Shanghai Jiao Tong University, Shanghai 200240, China*; orcid.org/0000-0002-6810-1380; Email: shangchaolin@sjtu.edu.cn

Authors

Huanhuan Zhou − *Department of Mechanical Engineering, Materials Science and Engineering Program, FAMU-FSU College of Engineering, Florida State University, Tallahassee, Florida 32310, United States*

Jingfan Wang − *Department of Mechanical Engineering, Materials Science and Engineering Program, FAMU-FSU College of Engineering, Florida State University, Tallahassee, Florida 32310, United States*

Complete contact information is available at: https://pubs.acs.org/10.1021/acsami.0c03532

Notes

The authors declare no competing financial interest.

■ ACKNOWLEDGMENTS

We would like to acknowledge the startup grant from Shanghai Jiao Tong University and the financial support from the National Science Foundation of the United States (#1708968).

■ REFERENCES

(1) Burschka, J.; Pellet, N.; Moon, S.-J.; Humphry-Baker, R.; Gao, P.; Nazeeruddin, M. K.; Grätzel, M. Sequential Deposition as A Route to High-Performance Perovskite-Sensitized Solar Cells. *Nature* **2013**, *499*, 316−319.

(2) Liu, M.; Johnston, M. B.; Snaith, H. J. Efficient Planar Heterojunction Perovskite Solar Cells by Vapour Deposition. *Nature* **2013**, *501*, 395−398.

(3) Stranks, S. D.; Snaith, H. J. Metal-Halide Perovskites for Photovoltaic and Light-Emitting Devices. *Nat. Nanotechnol.* **2015**, *10*, 391−402.

(4) Kumar, S.; Jagielski, J.; Yakunin, S.; Rice, P.; Chiu, Y.-C.; Wang, M.; Nedelcu, G.; Kim, Y.; Lin, S.; Santos, E. J. G.; Kovalenko, M. V.; Shih, C.-J. Efficient Blue Electroluminescence Using Quantum-Confined Two-Dimensional Perovskites. *ACS Nano* **2016**, *10*, 9720−9729.

(5) Etgar, L.; Gao, P.; Xue, Z.; Peng, Q.; Chandiran, A. K.; Liu, B.; Nazeeruddin, M. K.; Grätzel, M. Mesoscopic $CH_3NH_3PbI_3/TiO_2$ Heterojunction Solar Cells. *J. Am. Chem. Soc.* **2012**, *134*, 17396−17399.

(6) Ball, J. M.; Lee, M. M.; Hey, A.; Snaith, H. J. Low-Temperature Processed Meso-Superstructured to Thin-Film Perovskite Solar Cells. *Energy Environ. Sci.* **2013**, *6*, 1739−1743.

(7) Kojima, A.; Teshima, K.; Shirai, Y.; Miyasaka, T. Organometal Halide Perovskites as Visible-Light Sensitizers for Photovoltaic Cells. *J. Am. Chem. Soc.* **2009**, *131*, 6050−6051.

(8) Dong, Q.; Fang, Y.; Shao, Y.; Mulligan, P.; Qiu, J.; Cao, L.; Huang, J. Electron-Hole Diffusion Lengths > 175 mm in Solution-Grown $CH_3NH_3PbI_3$ Single Crystals. *Science* **2015**, *347*, 967−970.

(9) Matsumoto, F.; Vorpahl, S. M.; Banks, J. Q.; Sengupta, E.; Ginger, D. S. Photodecomposition and Morphology Evolution of Organometal Halide Perovskite Solar Cells. *J. Phys. Chem. C* **2015**, *119*, 20810−20816.

(10) Niu, G.; Guo, X.; Wang, L. Review of Recent Progress in Chemical Stability of Perovskite Solar Cells. *J. Mater. Chem. A* **2015**, *3*, 8970−8980.

(11) Akbulatov, A. F.; Luchkin, S. Y.; Frolova, L. A.; Dremova, N. N.; Gerasimov, K. L.; Zhidkov, I. S.; Anokhin, D. V.; Kurmaev, E. Z.; Stevenson, K. J.; Troshin, P. A. Probing the Intrinsic Thermal and Photochemical Stability of Hybrid and Inorganic Lead Halide Perovskites. *J. Phys. Chem. Lett.* **2017**, *8*, 1211−1218.

(12) Niu, G.; Li, W.; Meng, F.; Wang, L.; Dong, H.; Qiu, Y. Study on the Stability of $CH_3NH_3PbI_3$ Films and the Effect of Post-Modification by Aluminum Oxide in All-Solid-State Hybrid Solar Cells. *J. Mater. Chem. A* **2014**, *2*, 705−710.

(13) Yang, J.; Siempelkamp, B. D.; Liu, D.; Kelly, T. L. Investigation of $CH_3NH_3PbI_3$ Degradation Rates and Mechanisms in Controlled Humidity Environments Using in Situ Techniques. *ACS Nano* **2015**, *9*, 1955−1963.

(14) Leguy, A. M. A.; Hu, Y.; Campoy-Quiles, M.; Alonso, M. I.; Weber, O. J.; Azarhoosh, P.; van Schilfgaarde, M.; Weller, M. T.; Bein, T.; Nelson, J.; Docampo, P.; Barnes, P. R. F. Reversible Hydration of $CH_3NH_3PbI_3$ in Films, Single Crystals, and Solar Cells. *Chem. Mater.* **2015**, *27*, 3397−3407.

(15) Frost, J. M.; Butler, K. T.; Brivio, F.; Hendon, C. H.; van Schilfgaarde, M.; Walsh, A. Atomistic Origins of High-Performance in Hybrid Halide Perovskite Solar Cells. *Nano Lett.* **2014**, *14*, 2584−2590.

(16) Gottesman, R.; Haltzi, E.; Gouda, L.; Tirosh, S.; Bouhadana, Y.; Zaban, A.; Mosconi, E.; De Angelis, F. Extremely Slow Photo-

conductivity Response of $CH_3NH_3PbI_3$ Perovskites Suggesting Structural Changes under Working Conditions. *J. Phys. Chem. Lett.* **2014**, *5*, 2662−2669.
(17) Gottesman, R.; Zaban, A. Perovskites for Photovoltaics in the Spotlight: Photoinduced Physical Changes and Their Implications. *Acc. Chem. Res.* **2016**, *49*, 320−329.
(18) Zhang, L.; Sit, P. H.-L. Ab Initio Study of Interaction of Water, Hydroxyl Radicals, and Hydroxide Ions with CH3NH3PbI3 and CH3NH3PbBr3 Surfaces. *J. Phys. Chem. C* **2015**, *119*, 22370−22378.
(19) Koocher, N. Z.; Saldana-Greco, D.; Wang, F.; Liu, S.; Rappe, A. M. Polarization Dependence of Water Adsorption to $CH_3NH_3PbI_3$ (001) Surfaces. *J. Phys. Chem. Lett.* **2015**, *6*, 4371−4378.
(20) Mosconi, E.; Azpiroz, J. M.; De Angelis, F. Ab Initio Molecular Dynamics Simulations of Methylammonium Lead Iodide Perovskite Degradation by Water. *Chem. Mater.* **2015**, *27*, 4885−4892.
(21) Zhang, L.; Ju, M.-G.; Liang, W. The Effect of Moisture on The Structures and Properties of Lead Halide Perovskites: A First-Principles Theoretical Investigation. *Phys. Chem. Chem. Phys.* **2016**, *18*, 23174−23183.
(22) Tong, C.-J.; Geng, W.; Tang, Z.-K.; Yam, C.-Y.; Fan, X.-L.; Liu, J.; Lau, W.-M.; Liu, L.-M. Uncovering the Veil of the Degradation in Perovskite $CH_3NH_3PbI_3$ upon Humidity Exposure: A First-Principles Study. *J. Phys. Chem. Lett.* **2015**, *6*, 3289−3295.
(23) Caddeo, C.; Saba, M. I.; Meloni, S.; Filippetti, A.; Mattoni, A. Collective Molecular Mechanisms in the CH3NH3PbI3 Dissolution by Liquid Water. *ACS Nano* **2017**, *11*, 9183−9190.
(24) Mattoni, A.; Filippetti, A.; Saba, M. I.; Delugas, P. Methylammonium Rotational Dynamics in Lead Halide Perovskite by Classical Molecular Dynamics: The Role of Temperature. *J. Phys. Chem. C* **2015**, *119*, 17421−17428.
(25) MacKerell, A. D., Jr.; Banavali, N.; Foloppe, N. Development and Current Status of the CHARMM Force Field for Nucleic Acids. *Biopolymers* **2000**, *56*, 257−265.
(26) Cornell, W. D.; Cieplak, P.; Bayly, C. I.; Gould, I. R.; Merz, K. M.; Ferguson, D. M.; Spellmeyer, D. C.; Fox, T.; Caldwell, J. W.; Kollman, P. A. A Second Generation Force Field for the Simulation of Proteins, Nucleic Acids, and Organic Molecules. *J. Am. Chem. Soc.* **1995**, *117*, 5179−5197.
(27) Jorgensen, W. L.; Maxwell, D. S.; Tirado-Rives, J. Development and Testing of the OPLS All-Atom Force Field on Conformational Energetics and Properties of Organic Liquids. *J. Am. Chem. Soc.* **1996**, *118*, 11225−11236.
(28) Leijtens, T.; Bush, K.; Cheacharoen, R.; Beal, R.; Bowring, A.; McGehee, M. D. Towards Enabling Stable Lead Halide Perovskite Solar Cells; Interplay between Structural, Environmental, and Thermal Stability. *J. Mater. Chem. A* **2017**, *5*, 11483−11500.
(29) Chen, J.; Cai, X.; Yang, D.; Song, D.; Wang, J.; Jiang, J.; Ma, A.; Lv, S.; Hu, M. Z.; Ni, C. Recent progress in stabilizing hybrid perovskites for solar cell applications. *J. Power Sources* **2017**, *355*, 98−133.
(30) Yang, S.; Wang, Y.; Liu, P.; Cheng, Y.-B.; Zhao, H. J.; Yang, H. G. Functionalization of perovskite thin films with moisture-tolerant molecules. *Nat. Energy* **2016**, *1*, 15016.
(31) Li, X.; Ibrahim Dar, M.; Yi, C.; Luo, J.; Tschumi, M.; Zakeeruddin, S. M.; Nazeeruddin, M. K.; Han, H.; Grätzel, M. Improved performance and stability of perovskite solar cells by crystal crosslinking with alkylphosphonic acid ω-ammonium chlorides. *Nat. Chem.* **2015**, *7*, 703−711.
(32) Wang, F.; Geng, W.; Zhou, Y.; Fang, H.-H.; Tong, C.-J.; Loi, M. A.; Liu, L.-M.; Zhao, N. Phenylalkylamine Passivation of Organolead Halide Perovskites Enabling High-Efficiency and Air-Stable Photovoltaic Cells. *Adv. Mater.* **2016**, *28*, 9986−9992.
(33) Javaid, S.; Myung, C. W.; Pourasad, S.; Rakshit, B.; Kim, K. S.; Lee, G. A Highly Hydrophobic Fluorographene-Based System as An Interlayer for Electron Transport in Organic−Inorganic Perovskite Solar Cells. *J. Mater. Chem. A* **2018**, *6*, 18635−18640.
(34) Fu, Y.; Wu, T.; Wang, J.; Zhai, J.; Shearer, M. J.; Zhao, Y.; Hamers, R. J.; Kan, E.; Deng, K.; Zhu, X.-Y.; Jin, S. Stabilization of the Metastable Lead Iodide Perovskite Phase via Surface Functionalization. *Nano Lett.* **2017**, *17*, 4405−4414.
(35) Quan, L. N.; Yuan, M.; Comin, R.; Voznyy, O.; Beauregard, E. M.; Hoogland, S.; Buin, A.; Kirmani, A. R.; Zhao, K.; Amassian, A.; Kim, D. H.; Sargent, E. H. Ligand-Stabilized Reduced-Dimensionality Perovskites. *J. Am. Chem. Soc.* **2016**, *138*, 2649−2655.
(36) Chen, Y.; Sun, Y.; Peng, J.; Tang, J.; Zheng, K.; Liang, Z. 2D Ruddlesden-Popper Perovskites for Optoelectronics. *Adv. Mater.* **2018**, *30*, 1703487.
(37) Jana, A.; Ba, Q.; Kim, K. S. Compositional and Dimensional Control of 2D and Quasi-2D Lead Halide Perovskites in Water. *Adv. Funct. Mater.* **2019**, *29*, 1900966.
(38) Stoumpos, C. C.; Cao, D. H.; Clark, D. J.; Young, J.; Rondinelli, J. M.; Jang, J. I.; Hupp, J. T.; Kanatzidis, M. G. Ruddlesden−Popper Hybrid Lead Iodide Perovskite 2D Homologous Semiconductors. *Chem. Mater.* **2016**, *28*, 2852−2867.
(39) Lemmerer, A.; Billing, D. G. Synthesis, Characterization and Phase Transitions of the Inorganic-Organic Layered Perovskite-Type Hybrids $[(C_nH_{2n+1}NH_3)_2PbI_4]$, n = 7, 8, 9 and 10. *Dalton Trans.* **2012**, *41*, 1146−1157.
(40) Jana, A.; Kim, K. S. Water-Stable, Fluorescent Organic−Inorganic Hybrid and Fully Inorganic Perovskites. *ACS Energy Lett.* **2018**, *3*, 2120−2126.
(41) Li, B.; Kawakita, Y.; Liu, Y.; Wang, M.; Matsuura, M.; Shibata, K.; Ohira-Kawamura, S.; Yamada, T.; Lin, S.; Nakajima, K.; Liu, S. Polar Rotor Scattering as Atomic-Level Origin of Low Mobility and Thermal Conductivity of Perovskite $CH_3NH_3PbI_3$. *Nat. Commun.* **2017**, *8*, 16086.
(42) Yu, J.; Wang, M.; Lin, S. Probing the Soft and Nanoductile Mechanical Nature of Single and Polycrystalline Organic−Inorganic Hybrid Perovskites for Flexible Functional Devices. *ACS Nano* **2016**, *10*, 11044−11057.
(43) Wang, M.; Lin, S. Anisotropic and Ultralow Phonon Thermal Transport in Organic−Inorganic Hybrid Perovskites: Atomistic Insights into Solar Cell Thermal Management and Thermoelectric Energy Conversion Efficiency. *Adv. Funct. Mater.* **2016**, *26*, 5297−5306.
(44) Wang, J.; Zhao, L.; Wang, M.; Lin, S. Molecular Insights into Early Nuclei and Interfacial Mismatch during Vapor Deposition of Hybrid Perovskites on Titanium Dioxide Substrate. *Cryst. Growth Des.* **2017**, *17*, 6201−6211.
(45) Liu, S.; Cohen, R. E. Response of Methylammonium Lead Iodide to External Stimuli and Caloric Effects from Molecular Dynamics Simulations. *J. Phys. Chem. C* **2016**, *120*, 17274−17281.
(46) Handley, C. M.; Freeman, C. L. A new potential for methylammonium lead iodide. *Phys. Chem. Chem. Phys.* **2017**, *19*, 2313−2321.
(47) Gale, J. D.; Rohl, A. L. The General Utility Lattice Program (GULP). *Mol. Simul.* **2003**, *29*, 291−341.
(48) Berendsen, H. J. C.; Grigera, J. R.; Straatsma, T. P. The Missing Term in Effective Pair Potentials. *J. Phys. Chem.* **1987**, *91*, 6269−6271.
(49) Ponder, J. W.; Case, D. A. Force Fields for Protein Simulations. *Adv. Protein Chem.* **2003**, *66*, 27−85.
(50) Liu, M.; Johnston, M. B.; Snaith, H. J. Efficient planar heterojunction perovskite solar cells by vapour deposition. *Nature* **2013**, *501*, 395−398.
(51) McDonald, N. A.; Duffy, E. M.; Jorgensen, W. L. Monte Carlo Investigations of Selective Anion Complexation by a Bis(phenylurea)-p-tert-Butylcalix[4]arene. *J. Am. Chem. Soc.* **1998**, *120*, 5104−5111.
(52) Hockney, R. W.; Eastwood, J. W. *Computer Simulation Using Particles*; CRC Press, 1988.
(53) Allen, M. P.; Tildesley, D. J. *Computer Simulation of Liquids*; Oxford University Press, 1989.
(54) Plimpton, S. Fast Parallel Algorithms for Short-Range Molecular Dynamics. *J. Comput. Phys.* **1995**, *117*, 1−19.
(55) Parrinello, M.; Rahman, A. Polymorphic Transitions in Single Crystals: A New Molecular Dynamics Method. *J. Appl. Phys.* **1981**, *52*, 7182−7190.

https://dx.doi.org/10.1021/acsami.0c03532
ACS Appl. Mater. Interfaces 2020, 12, 23584−23594

(56) Nosé, S. A Unified Formulation of the Constant Temperature Molecular Dynamics Methods. *J. Chem. Phys.* **1984**, *81*, 511−519.
(57) Hoover, W. G. Canonical Dynamics: Equilibrium Phase-Space Distributions. *Phys. Rev. A* **1985**, *31*, 1695−1697.
(58) Walsh, A.; Scanlon, D. O.; Chen, S.; Gong, X. G.; Wei, S.-H. Self-Regulation Mechanism for Charged Point Defects in Hybrid Halide Perovskites. *Angew. Chem., Int. Ed.* **2015**, *54*, 1791−1794.
(59) Liu, Y.; Palotas, K.; Yuan, X.; Hou, T.; Lin, H.; Li, Y.; Lee, S.-T. Atomistic Origins of Surface Defects in CH3NH3PbBr3 Perovskite and Their Electronic Structures. *ACS Nano* **2017**, *11*, 2060−2065.
(60) Javaid, S.; Myung, C. W.; Yun, J.; Lee, G.; Kim, K. S. Organic Cation Steered Interfacial Electron Transfer within Organic−Inorganic Perovskite Solar Cells. *J. Mater. Chem. A* **2018**, *6*, 4305−4312.
(61) Myung, C. W.; Lee, G.; Kim, K. S. La-doped $BaSnO_3$ Electron Transport Layer for Perovskite Solar Cells. *J. Mater. Chem. A* **2018**, *6*, 23071−23077.
(62) Hailegnaw, B.; Kirmayer, S.; Edri, E.; Hodes, G.; Cahen, D. Rain on Methylammonium Lead Iodide Based Perovskites: Possible Environmental Effects of Perovskite Solar Cells. *J. Phys. Chem. Lett.* **2015**, *6*, 1543−1547.
(63) Somasundaran, P.; Healy, T. W.; Fuerstenau, D. W. Surfactant Adsorption at the Solid-Liquid Interface-Dependence of Mechanism on Chain Length. *J. Phys. Chem.* **1964**, *68*, 3562−3566.
(64) del Rio, J. M.; Pombo, C.; Prieto, G.; Mosquera, V.; Sarmiento, F. Effect of Temperature and Alkyl Chain Length on the Micellar Properties of n-Alkyltrimethylammonium Bromides in a Low pH Medium. *J. Colloid Interface Sci.* **1995**, *172*, 137−141.
(65) Xu, Y.; Liu, Y.-L.; Liu, G.-S. Molecular Dynamics Simulation of Primary Ammonium Ions with Different Alkyl Chains on the Muscovite (001) Surface. *Int. J. Miner. Process.* **2015**, *145*, 48−56.
(66) Sammalkorpi, M.; Sanders, S.; Panagiotopoulos, A. Z.; Karttunen, M.; Haataja, M. Simulations of Micellization of Sodium Hexyl Sulfate. *J. Phys. Chem. B* **2011**, *115*, 1403−1410.
(67) Sanders, S. A.; Sammalkorpi, M.; Panagiotopoulos, A. Z. Atomistic Simulations of Micellization of Sodium Hexyl, Heptyl, Octyl, and Nonyl Sulfates. *J. Phys. Chem. B* **2012**, *116*, 2430−2437.
(68) Caddeo, C.; Marongiu, D.; Meloni, S.; Filippetti, A.; Quochi, F.; Saba, M.; Mattoni, A. Hydrophilicity and Water Contact Angle on Methylammonium Lead Iodide. *Adv. Mater. Interfaces* **2018**, *6*, 1801173.
(69) Okouchi, M.; Yamaji, Y.; Yamauchi, K. Contact Angle of Poly(alkyl methacrylate)s and Effects of the Alkyl Group. *Macromolecules* **2006**, *39*, 1156−1159.
(70) Chen, J.; Chang, B.; Oyola-Reynoso, S.; Wang, Z.; Thuo, M. Quantifying Gauche Defects and Phase Evolution in Self-Assembled Monolayers through Sessile Drops. *ACS Omega* **2017**, *2*, 2072−2084.

https://dx.doi.org/10.1021/acsami.0c03532
ACS Appl. Mater. Interfaces 2020, 12, 23584−23594